BATTERIES

A room temperature rechargeable Li_2O-based lithium-air battery enabled by a solid electrolyte

Alireza Kondori[1], Mohammadreza Esmaeilirad[1], Ahmad Mosen Harzandi[1], Rachid Amine[2], Mahmoud Tamadoni Saray[3], Lei Yu[4], Tongchao Liu[5], Jianguo Wen[4], Nannan Shan[2,6], Hsien-Hau Wang[2], Anh T. Ngo[2,6], Paul C. Redfern[2], Christopher S. Johnson[5], Khalil Amine[5,7,8], Reza Shahbazian-Yassar[3], Larry A. Curtiss[2]*, Mohammad Asadi[1]*

A lithium-air battery based on lithium oxide (Li_2O) formation can theoretically deliver an energy density that is comparable to that of gasoline. Lithium oxide formation involves a four-electron reaction that is more difficult to achieve than the one- and two-electron reaction processes that result in lithium superoxide (LiO_2) and lithium peroxide (Li_2O_2), respectively. By using a composite polymer electrolyte based on $Li_{10}GeP_2S_{12}$ nanoparticles embedded in a modified polyethylene oxide polymer matrix, we found that Li_2O is the main product in a room temperature solid-state lithium-air battery. The battery is rechargeable for 1000 cycles with a low polarization gap and can operate at high rates. The four-electron reaction is enabled by a mixed ion–electron-conducting discharge product and its interface with air.

There is growing interest in developing chemistries to replace currently available energy storage systems that mainly work based on intercalations (*1*–*3*). One area of study has been Li-O_2 batteries based on the formation of lithium peroxide (Li_2O_2), the result of a two-electron reaction between Li^+ and O_2, or disproportionation of lithium superoxide (LiO_2), the result of a one-electron reaction (*4*, *5*). A Li-O_2 battery cell based on the lithium oxide (Li_2O) formation and decomposition could in theory deliver a higher energy density because it is based on a four-electron reaction either through a direct electron transfer [Fig. 1, pathway (I)] or indirectly through disproportionation [Fig. 1, pathway (II)].

Li_2O is more difficult to achieve compared with its counterparts LiO_2 and Li_2O_2 because it involves breaking an O_2 bond during discharge and remaking an O_2 bond during charge. There have been several studies of Li-ion batteries based on reversible Li_2O formation from other lithium oxides (e.g., peroxide or superoxide) or a nitrate molten salt (*6*–*8*). Recently, a lithium nitrate/potassium nitrate ($LiNO_3$/KNO_3) eutectic molten salt has been used as the electrolyte in a Li-O_2 battery to reversibly form and decompose crystalline Li_2O in a four-electron transfer redox (E° = 2.9 V versus Li/Li^+) at elevated temperatures (*7*, *9*). An alternative approach to achieving the four-electron Li_2O reaction in a Li-O_2 battery is to use a cell based only on gas and solid phases to promote fast reaction kinetics by avoiding problems with interfacial resistance and O_2 solubility (*10*). This could enable Li_2O formation as in pathway (I) (Fig. 1) if there is a sufficient supply of Li cations and electrons. A critical aspect would be the initial formation of a LiO_2/Li_2O_2 phase, both components of which can be ionically and electronically conductive (*11*–*15*), and having an air interface as a source of O_2. This system could then provide the needed mixed electron/ionic conduction properties for electrochemical formation of Li_2O, resulting in an overall four-electron reaction as in pathway (I), as well as avoiding electrolyte instabilities (*16*, *17*). Such an approach to attaining a four-electron reaction for a Li-O_2 battery requires the development of a stable, solid-state electrolyte with good ionic conductivity that interfaces well with the cathode.

Although there has been much research on the development of solid-state electrolytes (SSEs) for Li-ion batteries (*18*–*22*), there has been much less work done for Li-O_2 batteries. Thus far, the SSEs used for Li-O_2 have been based on metal phosphates, show fairly low reversibility and cyclability, and have Li_2O_2 as the main product (*23*–*29*).

The SSE used in this work was synthesized using a silane-coupling agent, mPEO-TMS {3-[methoxy(polyethyleneoxy)$_{6-9}$ propyl]trimethoxysilane}, to chemically bond with $Li_{10}GeP_2S_{12}$ (LGPS) nanoparticles in a P LiTFSI matrix (supplementary materials, tion S1). The LGPS nanoparticles are highly conductive, Li-rich ionic conductors (*30*, *31*). In addition, we used mPEO-TMS because of (i) its similar molecular structure compared with PEO, which avoids any phase separation between them; (ii) its higher Li^+ transference number (t_{Li}^+) in a certain molecular weight range compared with that of PEO (*32*, *33*); and (iii) its –OCH_3 termination, which improves the electrochemical stability window and the Li anode stability of the synthesized SSE (*34*). In this composite polymer electrolyte (CPE), the LGPS nanoparticles with an average crystallite size of 17 ± 6 nm (supplementary materials, section S2.1) are connected to the mPEO-TMS chains by strong chemical bonding of S atoms in Li_2S groups in LGPS to the Si in mPEO-TMS, which protects the LGPS from potential decomposition at the Li metal anode and the active cathode interfaces (supplementary materials, fig. S1 and section S1.2).

This bonding is known to occur due to the similarity between O–H and S–Li bonds (*35*). To confirm this, we performed x-ray photoelectron spectroscopy experiments on the CPE (Fig. 2, A and B, and supplementary materials, fig. S4 and section S2.2). The peaks at 162.0 and 103.1 eV in the S 2*p* and Si 2*p* spectra (Fig. 2, A and B) correspond to the presence of the Si-S bond, which strongly proves the interaction between Si atoms in mPEO-TMS and S atoms in LGPS. The C 1*s*, O 1*s*, and S 2*p* spectra also confirm the presence of PEO, mPEO-TMS, LGPS, and LiTFSI.

To analyze the structural morphology and chemical composition of the electrolyte, we performed scanning electron microscopy (SEM), as shown in Fig. 2C (supplementary materials, section S2.3). The SEM image of the SSE shown in Fig. 2C reveals a porous polymer matrix with an average pore size of ~d = 500 nm (inset in Fig. 2C). The elemental composition analysis using energy-dispersive x-ray spectroscopy also shows the uniform dispersion of the elements in the CPE (supplementary materials, fig. S5 and section S2.3).

We investigated the electronic properties of the CPE, first by measuring ionic conductivity at room temperature using electrochemical impedance spectroscopy (supplementary materials, section S3) (*36*–*38*). The Nyquist plots fitted with the circuit shown in the inset of Fig. 1D indicate an ionic conductivity of 0.52 mS/cm at room temperature for the SSE (thickness of 138 μm), which is 10 times higher than

[1]Department of Chemical and Biological Engineering, Illinois Institute of Technology, Chicago, IL 60616, USA. [2]Materials Science Division, Argonne National Laboratory, Lemont, IL 60439, USA. [3]Department of Mechanical and Industrial Engineering, University of Illinois at Chicago, Chicago, IL 60607, USA. [4]Center for Nanoscale Materials, Argonne National Laboratory, Lemont, IL 60439, USA. [5]Chemical Sciences and Engineering Division, Argonne National Laboratory, Lemont, IL 60439, USA. [6]Department of Chemical Engineering, University of Illinois at Chicago, Chicago, IL 60607, USA. [7]Material Science and Engineering, Stanford University, Stanford, CA 94305, USA. [8]Institute for Research&Medical Consultations (IRMC), Imam Abdulrahman Bin Faisal University (IAU), Dammam, Saudi Arabia.
*Corresponding author. Email: curtiss@anl.gov (L.A.C.); m.asadi@iit.edu (M.A.)

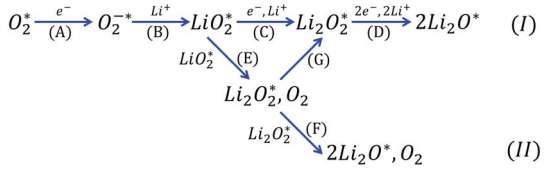

Fig. 1. Li_2O formation pathways. Shown are two reaction pathways to the formation of Li_2O based on the reaction of O_2, Li^+, and e^-.

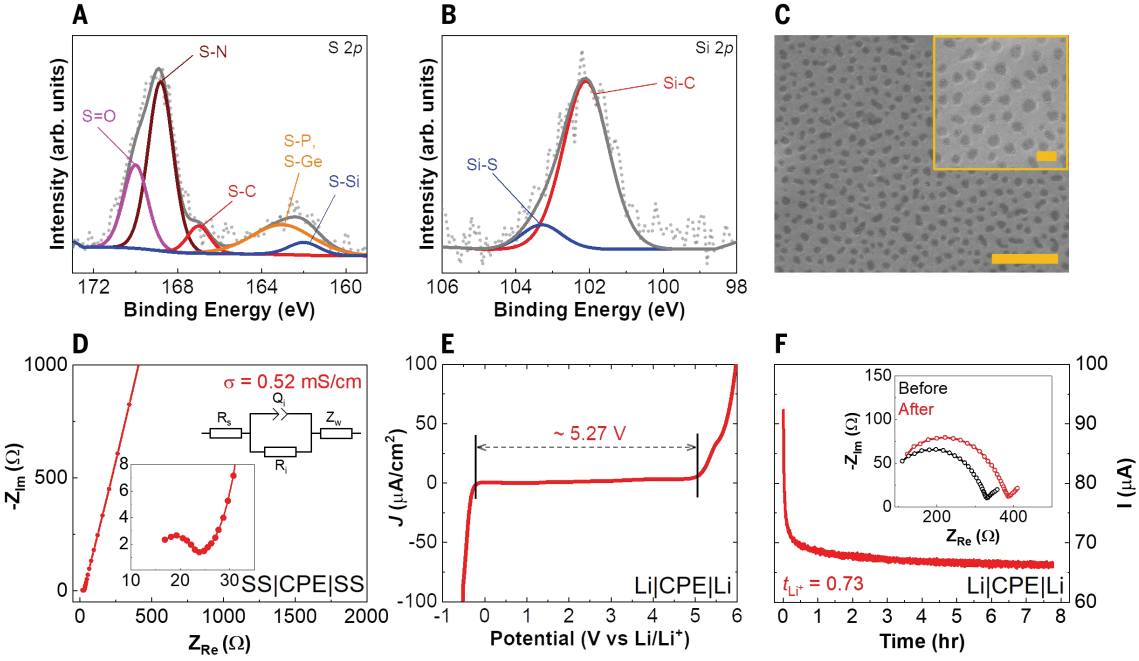

Fig. 2. Physicochemical and electrochemical characterization of the CPE. (**A**) S 2*p* and (**B**) Si 2*p* x-ray photoelectron spectroscopy of the CPE. (**C**) Low-magnification SEM image of the CPE (scale bar, 5 μm). The top right inset shows a high magnification of the SEM image, indicating an average pore size of 500 nm (scale bar, 1 μm). (**D**) Nyquist plot of the CPE indicating an ionic conductivity of ~0.52 mS/cm. The circuit used to fit the Nyquist plot of the CPE is shown in the inset of Fig. 1D. (**E** and **F**) Electrochemical redox stability of the CPE determined by a linear sweep voltammetry (LSV) experiment (E) and DC/AC analysis to measure the t_{Li+} of the CPE (F). The inset in this figure shows the electrochemical impedance spectroscopy spectra of the cell before and after applying a DC bias of 30 mV for ~8 hours.

that of the SSE without LGPS (i.e., PEO/mPEO-TMS/LiTFSI: 0.06 mS/cm; supplementary materials, fig. S6 and section S3). Moreover, the synthesized CPE exhibits ~15 times higher ionic conductivity compared with polymer electrolytes such as PEO with ionic conductivity of ~0.035 mS/cm at room temperature (*39*).

We measured the electrochemical stability of the SSE, which is a key factor to determining its practical application in Li batteries (supplementary materials, section S4). As shown in Fig. 1E, the CPE exhibits a large electrochemical redox stability window of 5.27 V. The high electrochemical stability of the CPE can be correlated to presence of $-OCH_3$ side chains in the mPEO-TMS, which form a stable interface with the Li metal anode (*34*).

Furthermore, we measured the Li transference number (t_{Li}^+) of the SSE with and without LGPS (supplementary materials, section S5) (*40*). The results shown in Fig. 1F indicate a t_{Li}^+ of 0.73 for the CPE that is ~2 times higher than that of the SSE without LGPS (t_{Li}^+ of 0.36; fig. S7). We attribute the improved t_{Li}^+ of the CPE to improved Li transport pathways, enabled by characteristic features of both the polymer and ceramic electrolytes and their interphase. This will provide three potential Li transport pathways (*41*, *42*), including those through (i) the bulk polymer matrix of PEO and mPEO-TMS, (ii) the bulk ceramic part (LGPS), and (iii) the newly formed interphase between LGPS and the mPEO-TMS. Moreover, using the silane-coupling agent ($Si-OCH_3$) group available in the mPEO-TMS, the LGPS nanoparticles are incorporated in the PEO matrix. This is known to eliminate the phase boundary between ethylene oxide–repeating units and the LGPS while reducing the grain boundary resistance between LGPS nanoparticles (*42*).

Performance analysis of the Li-air battery

The electrochemical performance of the CPE was examined in a custom-designed Li-air battery cell composed of a Li chip as the anode, the CPE as the SSE, and a cathode made up of trimolybdenum phosphide (Mo_3P) nanoparticles (*43*, *44*) loaded on a hydrophobic gas diffusion layer in an air-like atmosphere composed of 78% N_2, 21% O_2, ~45% relative humidity, and 500 ppm of CO_2 (supplementary materials, section S6.1). The capacity-limited cycling experiments were performed at room temperature under applied discharge and charge constant current densities of 1 A/g (0.1 mA/cm^2) and a capacity of 1 Ah/g measured based on the cathode material loading (0.1 mg/cm^2). For an example of a high cathode loading, see the supplementary materials, section S6.4.

Figure 3A shows the operation of the solid-state Li-air battery cell over 1000 cycles with charge and discharge potentials of 2.95 and 2.90 V compared with Li/Li$^+$ at the end of the first cycle, respectively. The charge and discharge voltage profiles of the solid-state Li-air battery cell over different cycles, i.e., 1, 200, 400, 600, 800, and 1000, are shown in Fig. 3B. The variations in coulombic efficiency (in red), energy efficiency (in green), and the polarization gap (in blue) of the solid-state Li-air battery cell are shown in Fig. 3C. Our measurements over the continuous cycling of the battery cell indicate a coulombic efficiency of 100% over 1000 cycles, with a polarization gap that increased from 50 mV at the first cycle to ~430 mV at the 1000th cycle. The energy efficiency of the first cycle was 92.7%, and it gradually dropped to 87.7% after 1000 cycles.

We also examined the rate capability of the developed battery cell at different rates including 2, 3, and 5 A/g (0.5 mA/cm^2) rates at a capacity of 0.5 mAh/cm^2 (supplementary materials, section S6.2). The results indicate that the solid-state Li-air battery can operate at faster rates; however, the polarization gap at the end of the first cycle became somewhat larger (fig. S8). Deep discharge capacity experiments also showed some losses at the higher rates (fig. S9).

Characterization of products

To characterize the chemistry of the cell and to identify discharge products in our developed solid-state Li-air battery cell, we first performed in situ Raman spectroscopy experiments (supplementary materials, section S7). Figure 4A shows the Raman spectra obtained at different time intervals (every 7.5 min or ~125 mAh/g) during the first discharge process (current density of 1 A/g, room temperature) compared with the pristine cathode. As shown in Fig. 4A, after the first 7.5 min of the discharge process, three new peaks appeared that are relevant to

the formation of LiO_2 (at ~1125 cm^{-1}), Li_2O_2 (at ~788 cm^{-1}), and Li_2O (at ~528 cm^{-1}) (*5*, *44*, *45*). This indicates that all of these species (LiO_2, Li_2O_2, and Li_2O) formed during the discharge process. To understand the interplay between the Li species that formed during discharge, we measured and compared the relative Raman peak intensities. The Li_2O peak intensity constantly increased over 1 hour of the discharge process (Fig. 4B). By contrast, the Li_2O_2 and LiO_2 peak intensities gradually increased during the initial time intervals, followed by a constant plateau during the rest of the discharge process. Raman spectroscopy results did not show any peaks associated with lithium hydroxide (LiOH) or lithium carbonate (Li_2CO_3) formation at the first discharge cycle. The in situ Raman spectroscopy experiments during the charge process also revealed that the Li_2O Raman peak disappeared after 1 hour of the charge process, whereas LiO_2 and Li_2O_2 Raman peaks disappeared after approximately half of the charge capacity (30 to 45 min) (supplementary materials, fig. S14 and section S7).

To gain more insight into the LiO_2/Li_2O_2 part of the discharge product, we performed a series of Raman spectroscopy experiments for the aged, discharged cathode under ultra-high-purity Ar and a vacuum environment (supplementary materials, section S7) to determine whether the LiO_2 would disproportionate (*46*). The Raman spectra of the aged samples (fig. S15) revealed that the signature Raman peak intensities associated with the LiO_2 (at 1125 and 1510 cm^{-1}) decreased with time, whereas the Raman peak intensity for Li_2O_2 increased under both Ar atmosphere and vacuum. These results confirm that disproportionation of LiO_2 to Li_2O_2 is favorable, with a slower disproportionation reaction under an Ar atmosphere. Moreover, after 5 days under the vacuum, the Raman spectrum of the discharged cathode indicated that the peak intensities associated with Li_2O_2 (788 cm^{-1}) increased, whereas none of the peaks relevant to the presence of LiO_2 (at 1125 and 1510 cm^{-1}) could be observed. This suggests that the LiO_2 and Li_2O_2 are on the outer surface of the discharge product, because the LiO_2 peak disappeared (and Li_2O_2

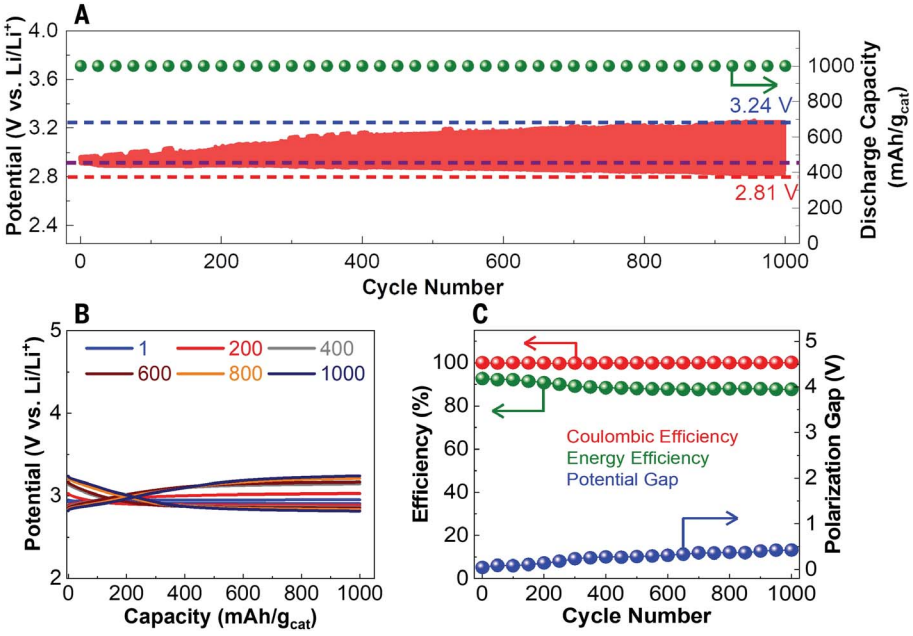

Fig. 3. Solid-state Li-air battery cell performance at a constant current density of 1 A/g and a limited capacity of 1 Ah/g. (**A**) Galvanostatic cycling over 1000 cycles. (**B**) Discharge/charge profiles at different cycles. (**C**) Coulombic efficiency (red dots), energy efficiency (green dots), and polarization gap at the end of cycle (blue dots) over 1000 cycles.

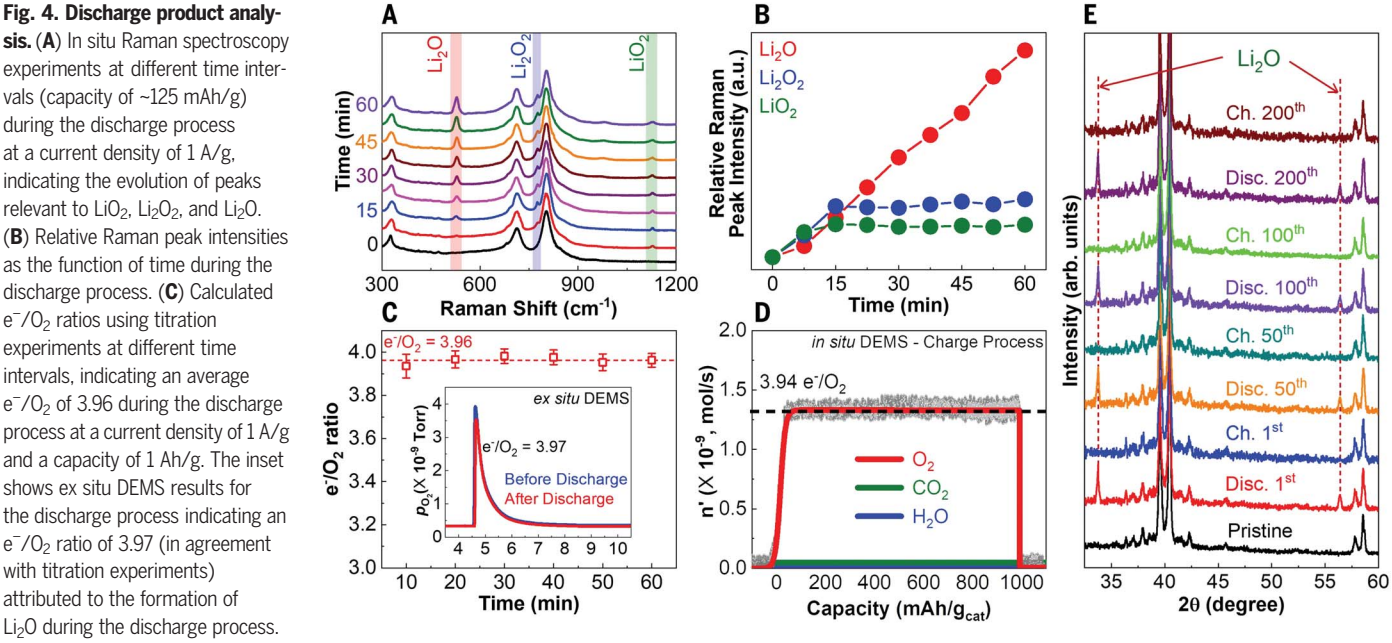

Fig. 4. Discharge product analysis. (**A**) In situ Raman spectroscopy experiments at different time intervals (capacity of ~125 mAh/g) during the discharge process at a current density of 1 A/g, indicating the evolution of peaks relevant to LiO_2, Li_2O_2, and Li_2O. (**B**) Relative Raman peak intensities as the function of time during the discharge process. (**C**) Calculated e^-/O_2 ratios using titration experiments at different time intervals, indicating an average e^-/O_2 of 3.96 during the discharge process at a current density of 1 A/g and a capacity of 1 Ah/g. The inset shows ex situ DEMS results for the discharge process indicating an e^-/O_2 ratio of 3.97 (in agreement with titration experiments) attributed to the formation of Li_2O during the discharge process. (**D**) In situ DEMS experiment for the charge process indicates an average e^-/O_2 of 3.94 at a constant current density of 5 A/g and a capacity of 1 Ah/g. (**E**) Thin-film diffraction patterns of the discharged/charged cathodes at different cycle numbers, i.e., 1, 50, 100, and 200, compared with the pristine cathode sample.

increased) with time and was dependent on whether the discharge product was in an Ar or a vacuum environment (*46*).

To further quantify the products formed during the discharge process, we performed titration coupled with ultraviolet-visible (UV-Vis) spectroscopy experiments as a function of discharge time (supplementary materials, section S8) (*6*, *9*, *46*, *47*). The titration results (Fig. 4C) indicated that an average electron to oxygen ratio (e^-/O_2) of 3.96 was transferred during the discharge process, suggesting that the discharge product is predominantly composed of Li_2O by an approximately four-electron transfer electrochemical reaction. These results suggest that the slight deviation from the theoretical e^-/O_2 ratio of 4.0 was due to the formation of small amounts of Li_2O_2 and LiO_2, as shown by the in situ Raman spectroscopy experiments shown in Fig. 4B. In addition, our results indicate that the total Li_2O formed over 30 min of the discharge process at a current density of 1 A/g was ~0.82 μmol (0.025 and 0.031 μmol for LiO_2 and Li_2O_2), which increased to ~1.77 μmol Li_2O over 60 min. The amount of LiO_2 and Li_2O_2 formed after 60 min of discharge process was ~0.023 and 0.032 μmol, respectively, much lower (two orders of magnitude) than that of Li_2O. Furthermore, these results indicate that the amount LiO_2 and Li_2O_2 remained almost unchanged over the last 30 min, whereas Li_2O predominantly increased during the discharge process, which is consistent with the in situ Raman spectroscopy experiments (Fig. 4, A and B).

The measured e^-/O_2 ratio obtained in our titration experiments was confirmed by performing ex situ and in situ differential electrochemical mass spectroscopy (DEMS) during the discharge and charge processes, respectively (supplementary materials, sections S9 and S10) (*5*, *44*, *45*). As shown in the inset of Fig. 4C, our ex situ DEMS experiment found an e^-/O_2 ratio of 3.97 over the discharge process, which is consistent with our titration experiments, confirming the formation of Li_2O as the discharge product in a nearly four-electron transfer reaction. The in situ DEMS experiment of the charge process (Fig. 3D) at a constant current density of 2.5 A/g and a capacity of 1 Ah/g showed an average e^-/O_2 of 3.94, which is quite close to that of the discharge process, meaning that the discharge product of the solid-state Li-air battery cell was reversibly decomposed. No change was observed in the CO_2 and H_2O signals of the DEMS, confirming the absence of species such as LiOH and Li_2CO_3 during the discharge process.

XRD experiments were performed to study the type and morphology of the discharge products in the solid-state Li-air battery cell and their reversibility with cycling (Fig. 4E and supplementary materials, section S11). Comparing the diffraction pattern of the discharged cathode at the first cycle with the pristine cathode showed two major peaks at 33.8° and 56.4° that were attributed to the (111) and (022) reflections of Li_2O crystals (*9*). No peaks were observed for either Li_2O_2 or LiO_2, which could be for one of two reasons: (i) there was only a small amount of deposited Li_2O_2 and LiO_2 as found by the UV-Vis experiments or (ii) that the deposited species were amorphous rather than crystalline. No characteristic peak related to that of Li_2CO_3 and LiOH was found in the diffraction patterns of the discharged cathodes. After the charge process of the first cycle, no characteristic peaks of Li_2O were observed, meaning that the Li_2O discharge product was fully removed by oxidation. This trend was similar in higher cycle numbers, e.g., 100 and 200.

We also compared the electrochemistry of the developed SSE with that of the liquid electrolyte in the Li-air battery cell using our previously developed liquid electrolyte with a Mo_3P-based cathode under identical experimental conditions (supplementary materials, section S12) (*44*). Characterization results for the discharged and charged cathodes of the liquid electrolyte Li-air battery cell indicated the reversible formation and decomposition of film-like Li_2O_2 (fig. S22). These results confirm that in the case of liquid electrolyte, the chemistry of the cell is mainly governed by the formation of Li_2O_2 in a two-electron reaction process, as opposed to a SSE battery, which favors nearly four-electron reaction chemistry by reversible formation and decomposition of Li_2O as the main product.

Elucidating the mechanism

The discharge mechanism in this solid-state Li-air battery has been deduced mainly on the basis of experimental results. The growth of the discharge products, including the major product, Li_2O, occurs in the space from incomplete contact between the cathode and CPE. Our AFM studies indicate that the cathode has roughness sufficient for space to exist (supplementary materials, fig. S23 and section S13). The cathode has pores ~40 nm in diameter for air flow (supplementary materials, figs. S24 and S25 and section S14). Additional experimental evidence used to deduce a growth mechanism is given in Fig. 5. This includes SEM images of the pristine cathode (Fig. 5A and fig. S24) and the discharged cathode (Fig. 5B and fig. S25, A and B) showing discharge product at the bottom of the "valleys" of the cathode structure. Also given in Fig. 5, C to F, are Raman mappings of different components of the discharged cathode (supplementary materials, section S15). These include Raman imaging of Mo_3P (Fig. 5D), Li_2O (Fig. 5E), and Li_2O_2 (Fig. 4F). It can be seen from Fig. 5, E and F, that the Li_2O and Li_2O_2 are located in the valleys and on the sides of the valleys. There was no LiO_2 in the Raman mapping because the cathode had been aged, which is consistent with our studies showing no LiO_2 in Raman after aging (supplementary materials, section S7). The Raman mapping of a nonaged sample is also shown in fig. S26. In addition, transmission electron microscopy (TEM) images of the discharge product indicate that some Mo_3P nanoparticles have an amorphous film 10 to 20 nm thick (Fig. 5, G and H), presumably the $LiO_2/Li_2O_2/Li_2O$ observed by the Raman mapping. In addition, there were large particles that were amorphous with some crystalline parts. Additional Raman spectroscopy and TEM results are given in figs. S26 and S32.

On the basis of the trends from acid-base titration coupled with UV-Vis experiments (fig. S20), all three products grew initially and then the amount of Li_2O_2 and LiO_2 reached a steady state after ~15 min (for a 60-min discharge). This is consistent with the in situ Raman peak intensities shown in Fig. 4B. The titration results indicate that LiO_2 and Li_2O_2 were each ~1% of the total discharge product by weight after 1 hour. The aging experiment (supplementary materials, section S7) discussed previously is evidence that the LiO_2 is on the surface of the discharge product, with the Li_2O_2 being in close proximity based on its Raman peak intensity increase with loss of LiO_2 on aging.

The predominance of the four-electron Li_2O reaction in this solid-state Li-air cell depends on the ionic and electronic conducting properties of the discharge product combined with the source of electrons (Mo_3P cathode), source of Li cations (CPE/Li anode), and abundance of O_2 (air). Moreover, with regard to the conducting properties of the discharge product, studies have shown that LiO_2 and Li_2O_2 can have good conductivity properties. Computational and experimental studies of LiO_2 have shown that it is electronically conducting (*11*, *48*), whereas computational studies have shown that amorphous Li_2O_2 has enhanced ionic conductivity (*12*) and that the surface of Li_2O_2 can have good electronic conductivity (*13*). It has also been shown in computational studies that amorphous Li_2O can be a fast ionic conductor (*49*). In addition, there may be nonstoichiometric Li_xO_y regions in the discharge product, because the reactions at the interfaces between stoichiometric compounds (LiO_2, Li_2O_2, and Li_2O) will not necessarily be the ideal ones shown by reaction I in Fig. 1. This is illustrated by the more detailed reaction I in Fig. 5J and could introduce more possibilities for ionic and electronic conductivity.

There are two growth stages of the discharge product, as illustrated in Fig. 5I: a pre–steady state and a steady state. After LiO_2/Li_2O_2 growth is initiated at a three-phase junction involving O_2 from air, Li^+ from the CPE, and

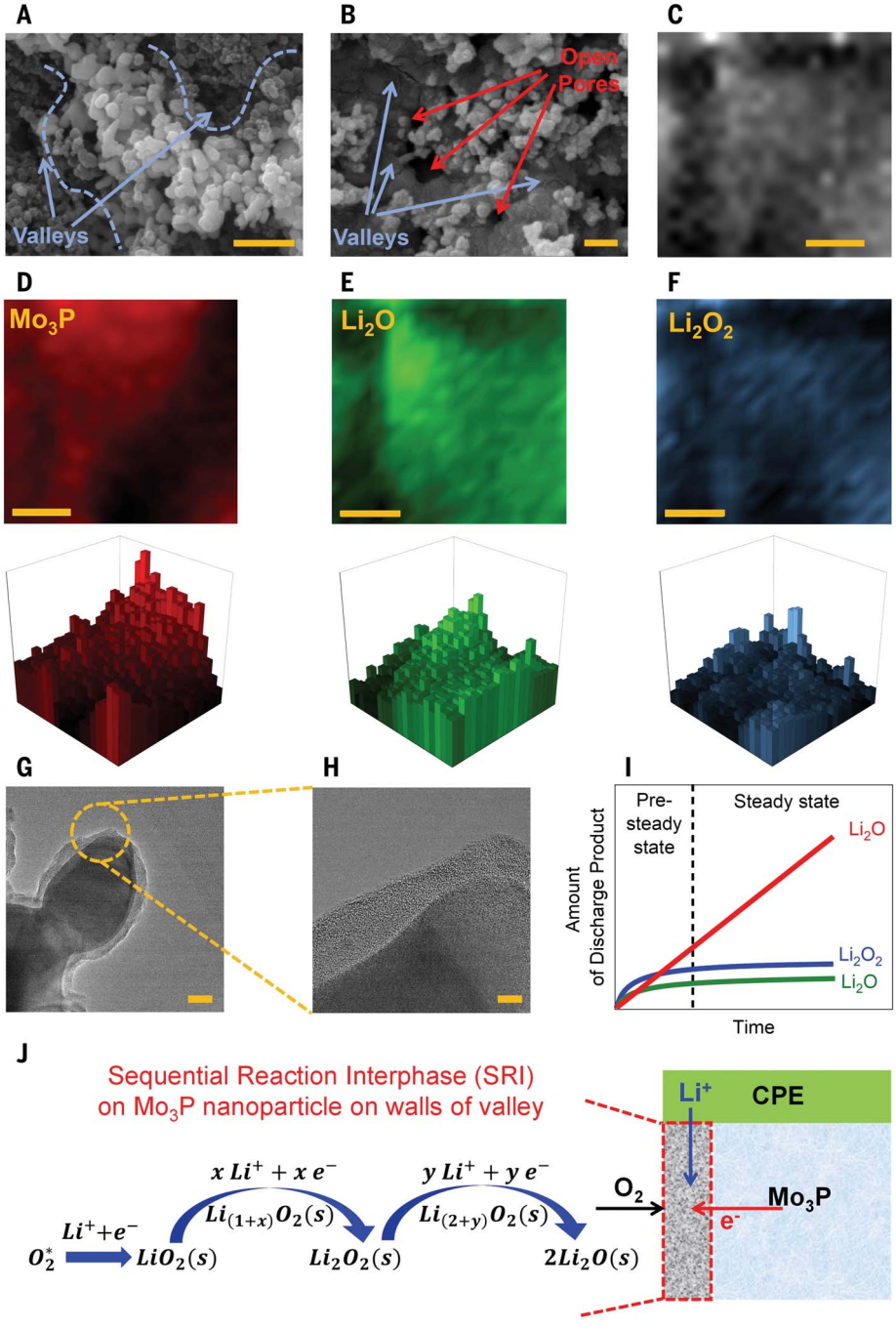

Fig. 5. Discharge reaction mechanism. (**A**) SEM image of a pristine cathode (scale bar, 500 nm); dashed blue lines show valleys. (**B**) SEM image of a discharged cathode (scale bar, 200 nm); blue arrows show the discharge products deposited in the valleys and red arrows show pores for air flow. (**C**) Raman microscope optical image [scale bars in (C) to (F), 1 μm] of the zone where the Raman maps shown in (D) to (F) were collected. (**D**) Two- and three-dimensional spatially resolved Raman mapping results of Mo_3P on the cathode surface. (**E**) Li_2O on the cathode surface. (**F**) Li_2O_2 on the cathode surface. (**G** and **H**) TEM images of the Mo_3P nanoparticle from the discharged cathode (scale bar, 20 nm) covered by the discharge product, which is an amorphous film ~10 to 20 nm thick [scale bars in (G) and (H), 5 nm]. (**I**) Diagram of discharge products as a function of time based on Raman spectra intensities. (**J**) Detailed reaction mechanism I (Fig. 1) for an SRI on a Mo_3P nanoparticle surface.

the Mo_3P cathode as an electrocatalyst, the LiO_2/Li_2O_2 will continue to grow. We performed density functional (DFT) calculations showing that O_2 has a binding on a LiO_2 surface (supplementary materials, section S16.2), which will enable steps A and B in reaction I (Fig. 1). The subsequent reaction of LiO_2 to Li_2O_2 occurs by the addition of a second electron and Li cation to LiO_2 (reaction I, Fig. 1, step C) or possibly by disproportionation of LiO_2 (reaction II, Fig. 1, step E). During the pre–steady-state phase (Fig. 5I), in addition to LiO_2 and Li_2O_2 growth, there will also be Li_2O formation from the last two electron/cation additions in reaction I (Fig. 1, step D). On the basis of the Raman peak intensities as a function of time (Fig. 4B), after ~15 min, the LiO_2 and Li_2O_2 reach a steady state and the Li_2O continues to grow due to excess Li cations. It has been speculated that disproportionation of Li_2O_2 (reaction II, Fig. 1, step F) may be a mechanism for the formation of Li_2O from Li_2O_2 (*9*). We do not believe that Li_2O_2 disproportionation occurs in a room temperature solid-state cell because the reaction is very endergonic, as shown by DFT calculations (supplementary materials, section S16). Thus, because LiO_2 is on the discharge product surface, it can regenerate while being a source for formation of Li_2O_2, which likewise can be a source for the formation of Li_2O (reaction II, Fig. 1, step D).

It is hypothesized that this set of sequential reactions will be forced to Li_2O by the abundance of O_2 at the gas-solid interface, excess Li cations due to the ionic conductivity of the CPE, and electronic conductivity of the cathode combined with the mixed electron-ion conductor nature of the amorphous phase of the discharge product, which we call a sequential reaction interphase. Figure 5J illustrates the sequential reactions occurring in

this amorphous phase on a Mo_3P nanoparticle. This could also occur in the bottoms of the valley (supplementary materials, fig. S33 and section S18.1). There is experimental evidence that supports this postulated sequential reaction mechanism in our solid-state Li-air battery. First, when the battery was run under the same conditions except for a liquid electrolyte, the reaction only proceeded to Li_2O_2, as already discussed. This is probably because of the availability of O_2 at the liquid-solid interface compared with the reactions in the amorphous phase, where no oxygen is present. Second, an Li-O_2 battery performed poorly with only PEO as a solid-state electrolyte (*50*), probably because the ionic conductivity of PEO at room temperature is much lower (*39*). Third, we have performed several restart experiments in which the cell was run for 30 min and then allowed to age for 5 days in a vacuum to allow LiO_2 to disproportionate to Li_2O_2. In such cases, in which there is no Raman evidence for LiO_2, the battery still operates both for charge and discharge, although at a slightly higher or lower voltage, respectively (supplementary materials, fig. S34 and section S18.2). This is probably because of loss of some electronic conductivity from disproportionation of LiO_2. Finally, we also note that conversion of Li_2O_2 to Li_2O in liquid cells without O_2 has been shown to be possible under the right environments (*6*, *8*).

During charge, the in situ Raman peak intensities for the different products (supplementary materials, fig. S14 and section S7) reveal that a somewhat different mechanism is present, because there was no steady-state period for LiO_2/Li_2O_2 decomposition as there was for formation during discharge. Instead, the intensities indicate that the three products decomposed at different rates, with LiO_2 and Li_2O_2 intensities disappearing after 30 to 45 min. The decomposition likely occurs in the reverse steps of the sequential reaction in the initial stage of the charge reaction (supplementary materials, fig. S35 and section S18.3) because O_2 is detected in DEMS throughout the charge (Fig. 4D), but with nonstoichiometric components contributing to the charge mechanism after the LiO_2 and Li_2O_2 components have largely disappeared (supplementary materials, fig. S35 and section S18.3).

Our results demonstrate that an SSE in a Li-air battery can enable a room temperature, reversible, four-electron Li_2O reaction for 1000 cycles with a low polarization gap at a high rate that operates in air. We also investigated the potential of this solid-state Li-air battery by performing deep discharge–charge experiments (supplementary materials, section S6.3). The results shown in fig. S9 indicate that this solid-state Li-air battery cell can work up to a capacity of ~10.4 mAh/cm^2, resulting in a specific energy of ~685 Wh/kg_{cell}. In addition, the cell has a volumetric energy density of ~614 Wh/L_{cell} because it operates well in air with no deleterious effects (supplementary materials, section S6.3). Thus, Li-air battery architectures based on SSEs can be constructed that are conducive to a four-electron Li_2O reaction and provide a real opportunity to obtain a projected specific energy of >1 kWh/kg (volumetric energy density of 1000 Wh/L), which is beyond what is possible from Li-ion technology.

REFERENCES AND NOTES

1. Z. Peng, S.A. Freunberger, Y. Chen, P.G. Bruce, *Science* **337**, 563–566 (2012).
2. Y.-C. Lu *et al*., *Energy Environ. Sci.* **6**, 750–768 (2013).
3. Y. Li, J. Lu, *ACS Energy Lett.* **2**, 1370–1377 (2017).
4. W.-J. Kwak *et al*., *Chem. Rev.* **120**, 6626–6683 (2020).
5. J. Lu *et al*., *Nature* **529**, 377–382 (2016).
6. Y. Qiao, K. Jiang, H. Deng, H. Zhou, *Nat. Catal.* **2**, 1035–1044 (2019).
7. V. Giordani *et al*., *Nat. Chem.* **11**, 1133–1138 (2019).
8. Z. Zhu *et al*., *Nat. Energy* **1**, 16111 (2016).
9. C. Xia, C. Y. Kwok, L. F. Nazar, *Science* **361**, 777–781 (2018).
10. C. Zhao *et al*., *Angew. Chem.* **133**, 5885–5890 (2021).
11. N. R. Mathiesen, S. Yang, J. M. García-Lastra, T. Vegge, D. J. Siegel, *Chem. Mater.* **31**, 9156–9167 (2019).
12. F. Tian, M. D. Radin, D. J. Siegel, *Chem. Mater.* **26**, 2952–2959 (2014).
13. M. D. Radin, J. F. Rodriguez, F. Tian, D. J. Siegel, *J. Am. Chem. Soc.* **134**, 1093–1103 (2012).
14. R. Gao *et al*., *Nano Energy* **41**, 535–542 (2017).
15. S. Li, J. Liu, B. Liu, *Chem. Mater.* **29**, 2202–2210 (2017).
16. S. A. Freunberger *et al*., *J. Am. Chem. Soc.* **133**, 8040–8047 (2011).
17. N. Mahne *et al*., *Nat. Energy* **2**, 17036 (2017).
18. W. Liu *et al*., *Nat. Energy* **2**, 17035 (2017).
19. J. Wan *et al*., *Nat. Nanotechnol.* **14**, 705–711 (2019).
20. Y. Zhu *et al*., *Adv. Energy Mater.* **4**, 1300647 (2014).
21. Y. Wang *et al*., *Nat. Mater.* **14**, 1026–1031 (2015).
22. Z. Du *et al*., *J. Electrochem. Soc.* **168**, 050549 (2021).
23. B. Kumar *et al*., *J. Electrochem. Soc.* **157**, A50 (2010).
24. S. Wang *et al*., *J. Mater. Chem. A Mater. Energy Sustain.* **6**, 21248–21254 (2018).
25. Y. Liu *et al*., *ACS Appl. Mater. Interfaces* **7**, 17307–17310 (2015).
26. Y. Wang, H. Zhou, *Energy Environ. Sci.* **4**, 1704–1707 (2011).
27. H. Kitaura, H. Zhou, *Energy Environ. Sci.* **5**, 9077–9084 (2012).
28. X. Zhu, T. Zhao, P. Tan, Z. Wei, M. Wu, *Nano Energy* **26**, 565–576 (2016).
29. S. Hasegawa *et al*., *J. Power Sources* **189**, 371–377 (2009).
30. N. Kamaya *et al*., *Nat. Mater.* **10**, 682–686 (2011).
31. Y. Mo, S. P. Ong, G. Ceder, *Chem. Mater.* **24**, 15–17 (2012).
32. C. Zhang *et al*., *Nat. Mater.* **8**, 580–584 (2009).
33. Z. Gadjourova, Y. G. Andreev, D. P. Tunstall, P. G. Bruce, *Nature* **412**, 520–523 (2001).
34. X. Yang *et al*., *Energy Environ. Sci.* **13**, 1318–1325 (2020).
35. T.-Z. Hou *et al*., *Angew. Chem. Int. Ed.* **56**, 8178–8182 (2017).
36. X. Z. Yuan, C. Song, H. Wang, J. Zhang, *Electrochemical Impedance Spectroscopy in PEM Fuel Cells: Fundamentals and Applications* (Springer, 2010).
37. X. C. Chen *et al*., *ACS Energy Lett.* **4**, 1080–1085 (2019).
38. M. J. Palmer *et al*., *Energy Storage Mater.* **26**, 242–249 (2020).
39. N. H. A. M. Hashim, R. H. Y. Subban, *AIP Conf. Proc.* **2031**, 020021 (2018).
40. P. G. Bruce, J. Evans, C. A. Vincent, *Solid State Ion.* **28–30**, 918–922 (1988).
41. J. Ou, G. Li, Z. Chen, *J. Electrochem. Soc.* **166**, A1785–A1792 (2019).
42. K. Pan *et al*., *Adv. Mater.* **32**, e2000399 (2020).
43. A. Kondori *et al*., *Adv. Energy Mater.* **9**, 1900516 (2019).
44. A. Kondori *et al*., *Adv. Mater.* **32**, e2004028 (2020).
45. M. Asadi *et al*., *Nature* **555**, 502–506 (2018).
46. D. Zhai *et al*., *Nano Lett.* **15**, 1041–1046 (2015).
47. H. H. Wang *et al*., *J. Phys. Chem. C* **121**, 9657–9661 (2017).
48. S. T. Plunkett *et al*., *ACS Appl. Energy Mater.* **3**, 12575–12583 (2020).
49. J. S. Lowe, D. J. Siegel, *ACS Appl. Mater. Interfaces* **12**, 46015–46026 (2020).
50. J. Hassoun, F. Croce, M. Armand, B. Scrosati, *Angew. Chem. Int. Ed.* **50**, 2999–3002 (2011).

ACKNOWLEDGMENTS

Funding: M.A., R.A., K.A., T.L., A.N., C.J., and H.W. were supported by the US Department of Energy under contract DE-AC02-06CH11357 from the Vehicle Technologies Office, Office of Energy Efficiency and Renewable Energy. M.A. efforts were also partially supported by the Illinois Institute of Technology Armour College of Engineering, Wanger Institute for Sustainable Energy Research (WISER) seed fund (262029 221E 2300). N.S., P.R., and L.C. were supported by the Joint Center for Energy Storage Research (JCESR), an Energy Innovation Hub funded by the Office of Science, Basic Energy Sciences. R.S.Y. was supported by NSF grant DMR-1809439. Characterization Work by A.K., A.M.H., and M.E. was performed at the Keck-II facility of Northwestern University's NUANCE Center, which has received funding from the SHyNE Resource [National Science Foundation (NSF) grant ECCS-1542205]; the MRSEC program (NSF grant DMR-1720139) at the Materials Research Center; the International Institute for Nanotechnology (IIN); the Keck Foundation; and the State of Illinois through the IIN. Work by J.W. and Y.L. was performed at the Center for Nanoscale Materials, a US Department of Energy (DOE) Office of Science User Facility supported by the US DOE Office of Basic Energy Sciences under contract DE-AC02-06CH11357.
Author contributions: M.A. and A.K. conceived the idea. A.K., A.M.H., and M.E. synthesized the battery cell components, the cathode, and the SSE. A.K., A.M.H., and M.E. performed the battery cell run experiments. A.K. and M.E. performed the XRD, x-ray photoelectron spectroscopy, Raman spectroscopy, UV-Vis spectroscopy, DEMS, and electrochemical experiments. M.A. supervised the experimental efforts in design, synthesis, characterization, and electrochemical testing and analyses. C.J. helped with experimental design and analyses. M.T.S. and R.S.Y. performed SEM and energy-dispersive x-ray spectroscopy analyses of the cathode and the SSE. R.A., L.Y., T.L., J.W., H.W., and K.A. performed TEM and AFM experiments. N.S., P.R., and A.N. performed DFT calculations. L.C. helped with deducing the reaction mechanism based on the experimental observations and DFT calculations. All authors contributed to writing the manuscript.
Competing interests: M.A., A.K., and M.E. have filed a provisional patent application for the work described herein. The remaining authors declare no competing financial interests. **Data and materials availability:** All data are available in the main manuscript or the supplementary materials.

SUPPLEMENTARY MATERIALS

science.org/doi/10.1126/science.abq1347
Sections S1 to S18
Figs. S1 to S35
Tables S1 to S4
References (*51*–*75*)

Submitted 21 March 2022; accepted 23 November 2022
10.1126/science.abq1347

A room temperature rechargeable Li_2O-based lithium-air battery enabled by a solid electrolyte

Alireza Kondori, Mohammadreza Esmaeilirad, Ahmad Mosen Harzandi, Rachid Amine, Mahmoud Tamadoni Saray, Lei Yu, Tongchao Liu, Jianguo Wen, Nannan Shan, Hsien-Hau Wang, Anh T. Ngo, Paul C. Redfern, Christopher S. Johnson, Khalil Amine, Reza Shahbazian-Yassar, Larry A. Curtiss, and Mohammad Asadi

Science **379** (6631), . DOI: 10.1126/science.abq1347

An enabling composite electrolyte

Lithium-air batteries have scope to compete with gasoline in terms of energy density. However, in most systems, the reaction pathways either involve one- or two-electron transfer, leading to lithium peroxide (Li_2O_2) or lithium superoxide (LiO_2), respectively. Kondori *et al*. investigated a lithium-air battery that uses a ceramic-polyethylene oxide–based composite solid electrolyte and found that it can undergo a four-electron redox reaction through lithium oxide (Li_2O) formation and decomposition (see the Perspective by Dong and Lu). The composite electrolyte embedded with $Li_{10}GeP_2S_{12}$ nanoparticles shows high ionic conductivity and stability and high cycle stability through a four-electron transfer process. —MSL

Science (ISSN 1095-9203) is published by the American Association for the Advancement of Science. 1200 New York Avenue NW, Washington, DC 20005. The title *Science* is a registered trademark of AAAS.